Int J Adv Manuf Technol (2015) 79:2017–2030
DOI 10.1007/s00170-015-6948-y

ORIGINAL ARTICLE

Investigation of work hardening behavior and failure analysis of billets due to biaxial stresses in simple upsetting process

Ch. Hari Krishna · M. J Davidson · Ch. Nagaraju

Received: 11 October 2012 / Accepted: 23 February 2015 / Published online: 14 March 2015

Abstract The present work focuses on the work hardening behavior of the AA2014-T6 billets deformed plastically between two flat cylindrical rigid dies under cold working condition. Three sets of billets of different aspect ratios (height (h) to the diameter (d)), namely h/d=1, h/d=0.75, and h/d=0.5 were deformed to the different strain levels. Upon severe plastic deformation, the cylindrical billets will start cracking from the middle, and the crack will propagate to the surface. The hydrostatic stress and deviatoric stresses influence the failure of the billets resulting in poor ductility and distorting the shape of the billet. To analyze the effect of shear bands on the failure of the billet, maximum shear stress theory was applied. A detailed investigation has been carried out to study the influence of the tensile nature of the hoop stress, axial stress, and hydrostatic stresses. The critical paths for different aspect ratios of the deformed billets were plotted, and the failure of the specimen was well explained. The effect of anisotropy on the formability was studied by constituting the anisotropy factor with the ductile fracture models such as Gurson-Tvergaard-Needleman model and Lemaitre model. The influence of anisotropy on the void failure was studied, and critical damage was evaluated for different anisotropy ratios.

Keywords Ductile fracture · AA2014 aluminum alloy · Anisotropy · Tensile stresses · Critical paths · Void models

C. H. Krishna (✉) · C. Nagaraju
Department of Mechanical Engineering, V. R. Siddhartha Engineering College, Kanuru, Vijayawada, India 520007
e-mail: harinitw@gmail.com

M. J. Davidson
Department of Mechanical Engineering, National Institute of Technology, Warangal, India

1 Introduction

When the billet is cold worked then strain hardening of the material takes place. The increase in the stress required to cause metal flow is called strain hardening. To describe the work hardening behavior, the strain hardening exponent (n) and strain hardening coefficient (k) must be studied. Narayanasamy et al. [1] conducted studies on the work hardening behavior of the elliptical-shaped billets with different lengths of the major axis and minor axis and different height to the diameter ratios. They concluded that the instantaneous value of k and n varies with the height to the diameter ratios of the billets and also on the ratio of major axis to the minor axis. The increase in the deformation reduces the porosity level in the sintered powder preforms. The strain hardening coefficient and strain hardening exponent also depend on the size of the particles and their composition for porous materials. Similar studies were reported by Narayansamy et al. [2] while conducting experiments on the aluminum-iron composite performs. The stresses acting on the billets influence the formability of the material. Inigoraj [3] conducted experiments on the aluminum-alumina composite and developed a relation between strain hardening coefficient and theoretical density. The increase in the level of deformation reduces the porosity and increases the load-bearing capacity in powder preforms which increases the work hardening behavior [4]. Their research findings also report that after a small level of strain, the magnitude of the strain hardening exponent decreases. The Cu-5%W Nano powder Composite powder was used for preparing preforms of different height to the diameter ratios of 0.4, 0.60, and 0.80 and was axially compressed [5]. They concluded that upsetting powder preforms of lower height to the diameter ratios improve densification resulting in extensive work hardening.

Baskaran et al. conducted experiments on the cold forming of elliptical billets. They examined the effect of various stress

ratio parameters [6] on the barreling curvature of the elliptical billets under the state of biaxial and triaxial state of stresses and concluded that the rate of change of barrel radius changes with the state of stresses. Their research findings also proved that the barrel radius follows a power law with the stress ratio parameter [7]. Depending on the nature of lubrication condition applied on the faces of the billets, the geometry of the billets changes its shape in simple cylindrical upset forging process. The value of friction changes with the type of machining operation performed on the faces of the billet such as facing, milling, grinding, etc. [8] and also on the lubricant employed [9]. On employing different friction conditions on the faces by performing different machining operations and by applying different lubricants, Malayappan et al. carried out experiments on the solid cylindrical billets by compressing them in between the dies. Their studies revealed that different friction conditions at the faces of the billets lead to truncated shape, and this phenomenon continues with the increase in the level of deformation. The state of stresses, namely the hoop stress, the hydrostatic stress, and the effective stress, increases with the increase in the strain level and differs with the value of the barrel curvature. Fuh-Kuo et al. [10] developed a theoretical model for the flow stress based on the shape of the barrel. By deriving the equation for mean effective strain on the basis of assumed velocity fields, Fuh-Kuo constructed stress-strain curve and developed the flow stress equation. The theoretical equation proposed by him was in good agreement with the finite element results. The flow curves of the metals are normally predicted by a tensile test or a bulging test of the solid cylinders. Alves et al. [11] made useful contributions in developing the flow curves of sheet metals by utilizing stack compression tests. The results predicted using the stack compression tests were in close proximity with the standard compression test.

Several authors made experimental and finite element investigations on the analysis of ductile fractures in the bulk-forming and sheet metal operations. By employing ductile fracture models, Song et al. [12] conducted experiments and finite element simulations on the sheet metal operations. They concluded that the process parameter, such as clearance between the punch the die influences the fracture. The simulated results obtained by using element-deletion and replacement method incorporating the fracture models enabled them to study the crack initiation and propagation. The experimental studies in conjunction with the finite element results always have a better advantage in predicting the zones of fracture in the specimen. Li et al. [13] predicted the ductile fracture in AA6061-T6 test specimens by conducting tensile and compression tests and by applying coupled and uncoupled damage models. They notice that the coupled damage models are accurate in predicting the damaged portions of the specimen when compared to the uncoupled damage models. Application of artificial neural networks in combination with the finite element simulations can reduce the extent of experimentation. A similar study has been made by Kim et al. [14] to predict the ductile fracture in simple upsetting of solid cylindrical billets. They conclude that the artificial neural network could successfully predict the ductile fracture for arbitrary aspect ratios, and the methodology is also useful in predicting the critical damage values which is undone using finite element simulation.

The coupled damage criterion has been used by Pires et al. [15] for predicting the critical damage value. They explained the behavior of crack initiation and propagation phenomena and developed a numerical modeling for estimating the value of critical damage in bulk metal forming. The results thus obtained from numerical modeling were in agreement with the finite element and experimental results obtained. Gouveia et al. [16] conducted experiments on the flanged, tapered, and cylindrical specimens to determine the value of critical damage deformed under cold working condition. They employed uncoupled workability of criterions such as cockroft-Latham criterion [17], Freudenthal criterion [18], Brozzo criterion [19], and Oyane criterion [20] for predicting the critical damage value.

The strength of the material depends on the work hardening behavior of the material. The present work addresses about the work hardening behavior of AA2014-T6 billets because of the significance of the material in aerospace applications. The bibliography reported on the top describes the influences of stresses, workability criteria on the barreled specimens. The reason for the failure due to tensile stresses near the equatorial region, deviatoric stresses, and shear failures has been the limitation in the previous studies. The billets were deformed plastically till a small crack appears on the surface of the billet, and the deformation was carried out further for crack propagation. The failures due to various types of stresses have been clearly explained for better utilization of the material and processing conditions. The effect of anisotropy on the ductile fracture has been analyzed, and the anisotropy factor was modeled in constitution with the existing ductile fracture criterion such as Gurson-Tvergaard-Needleman and Lemaitre fracture criterion.

2 Experimental procedure

The aluminum alloy AA2014 procured from the supplier was in T6 condition in its natural form. This aluminum alloy was machined to different height to the diameter ratios. This is a widely used material in aerospace applications and AA2014-T6 has the ultimate tensile strength of 483 MPa and yield strength of 414 MPa. This alloy has a hardness (RHN-B) of 82 and percentage elongation of 13 %. The solid cylinders of different aspect ratios were used because the formability limit for different aspect ratios upon upsetting.

A series of solid cylindrical compression tests of different aspect ratios, namely h/d=1, h/d=0.75, and h/d=0.5, were conducted. The billets were reduced to different strain levels in between two rigid dies using a 50-ton capacity universal testing machine (Fig. 1). After each and every successive stage of the deformation process, the following sets of results were noted down as shown in Fig. 2.

D_b is bulged diameter near the equatorial region of the billet
D_c is contact diameter of the billet
h_o is the initial height of the billet
h_f is the final height of the billet

The work hardening exponent (n) and work hardening coefficient (k) were determined using Eqs. (1) and (2) proposed by Narayanasamy et al. [2] from the Ludwik equation.

$$\sigma = k\varepsilon^n \tag{1}$$

$$n = \ln(\sigma_m - \sigma_{m-1})/\ln(\varepsilon_m - \varepsilon_{m-1}) \tag{2}$$

$$k = (\sigma_m - \sigma_{m-1})/\varepsilon_m^n - \varepsilon_{m-1}^n \tag{3}$$

where σ_1, σ_2,…, σ_m and ε_1, ε_2,…, ε_m are the instantaneous values of true stresses and true strains, respectively. Depending on the state of stresses, the values of n and k are determined from the equations of Appendix A, Appendix B, and Appendix C.

2.1 Effecting stress factors

To investigate the formability of the material, the material plays a significant rule. Apart from the processing conditions, the various types of stresses, namely hydrostatic stresses (σ_m), shear stresses (τ), and deviatoric stresses, namely $\sigma_1^{|}$, $\sigma_2^{|}$, will also influence the workability of the materials. The hydrostatic stresses are responsible for the improving ductility of the material, and the tensile nature of the hydrostatic stress promotes fracture. The deviatoric stresses influence the shape change of the geometry. While the deformation is going on, the shear zones may develop because of the localized deformation of the material. These shear zones will initiate minute cracks, and this may lead to the surface fractures. On achieving higher deformations, the geometry of the billet tends to barrel and promotes biaxial state of stresses. The biaxial stress state, which develops at the equatorial region, comprises the axial stresses (σ_z) and hoop stresses (σ_θ) [14].

Fig. 1 Billets of different aspect ratios (h/d) after upsetting to the fracture limit

When the billets were reduced to different heights, the crack initiation and propagation of the specimens were examined. The following equations were used to determine the values of the deviatoric stresses, maximum shear stresses, and hydrostatic stresses assuming biaxial stress state condition which is responsible for the failure due to barreling of the cylinders near the equatorial region.

$$\text{Deviatoric stress } \sigma_1 = \sigma_z - \sigma_m \tag{4}$$

$$\text{Deviatoric stress } \sigma_2 = \sigma_\theta - \sigma_m \tag{5}$$

$$\text{Hydrostatic stress } \sigma_m = (\sigma_\theta + \sigma_z)/3 \tag{6}$$

$$\text{Maximum shear stress } \tau_{\max} = (\sigma_\theta - \sigma_z)/2 \tag{7}$$

3 Results and discussions

3.1 Work hardening behavior

It can be examined from Fig. 3 that the increase in the value of the axial strain increases the value of the strain hardening exponent (n). In general, the value of n which can be determined from the slope of the plot of $\ln(\sigma)$ versus $\ln(\varepsilon)$. The instantaneous increase in the value of true strain also increases the true stress. The rate of change of true stress with respect to the true strain increases with the increasing deformation level. This will affect the value of n, and the rate of change of n with respect to the axial strain was minor at lower strain and major at higher strain values. A similar phenomenon has been observed irrespective of all the aspect ratios and state of stresses.

The value of the strength coefficient depends on the values of the true stress and true strain which in turn depend on the load-stroke diagram of the billets. The increase in the load increases the amount of stress and strain. At the beginning of the process, the value of the stress is less, and it creeps as the value of the strain increases. This makes a noticeable change in the strain hardening exponent, and its value

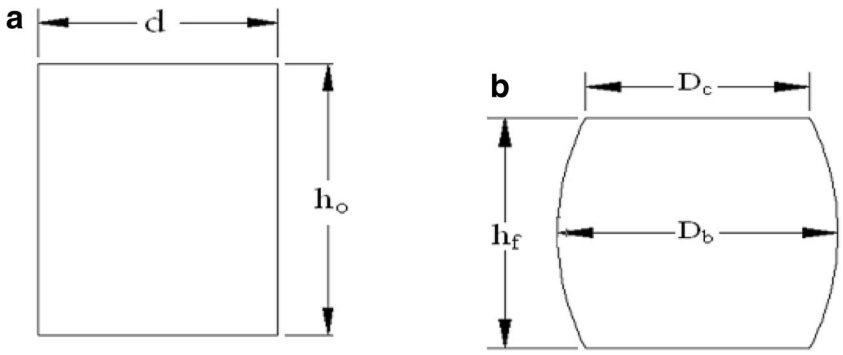

Fig. 2 Geometry of the billet **a** before and **b** after deformation

increases with the increasing axial strain. Similar phenomenon is examined for all the state of stresses and aspect ratios as illustrated in Fig. 4. As explained by Baskaran et al. [1], the strain hardening experienced by the billet changes with the magnitude of the strain because of the factors such as material, friction at the die/billet interface, and billet geometry.

3.2 Failure analysis

The increase in the strength coefficient increases the brittleness of the material and reduces the formability of the billets. After discussing the work hardening behavior of the billets, the stresses responsible for the

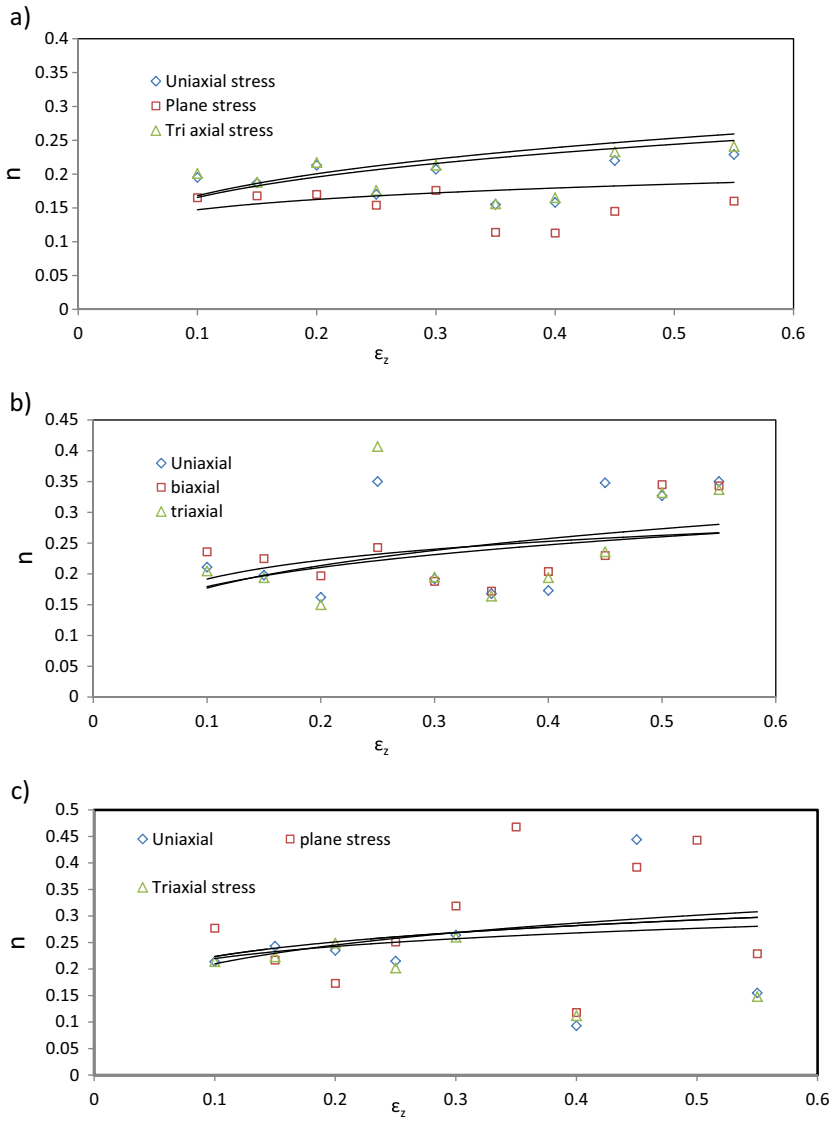

Fig. 3 Variation of instantaneous value of n with the axial strain ε_z for **a** h/d=1, **b** h/d=0.75, and **c** h/d=0.5

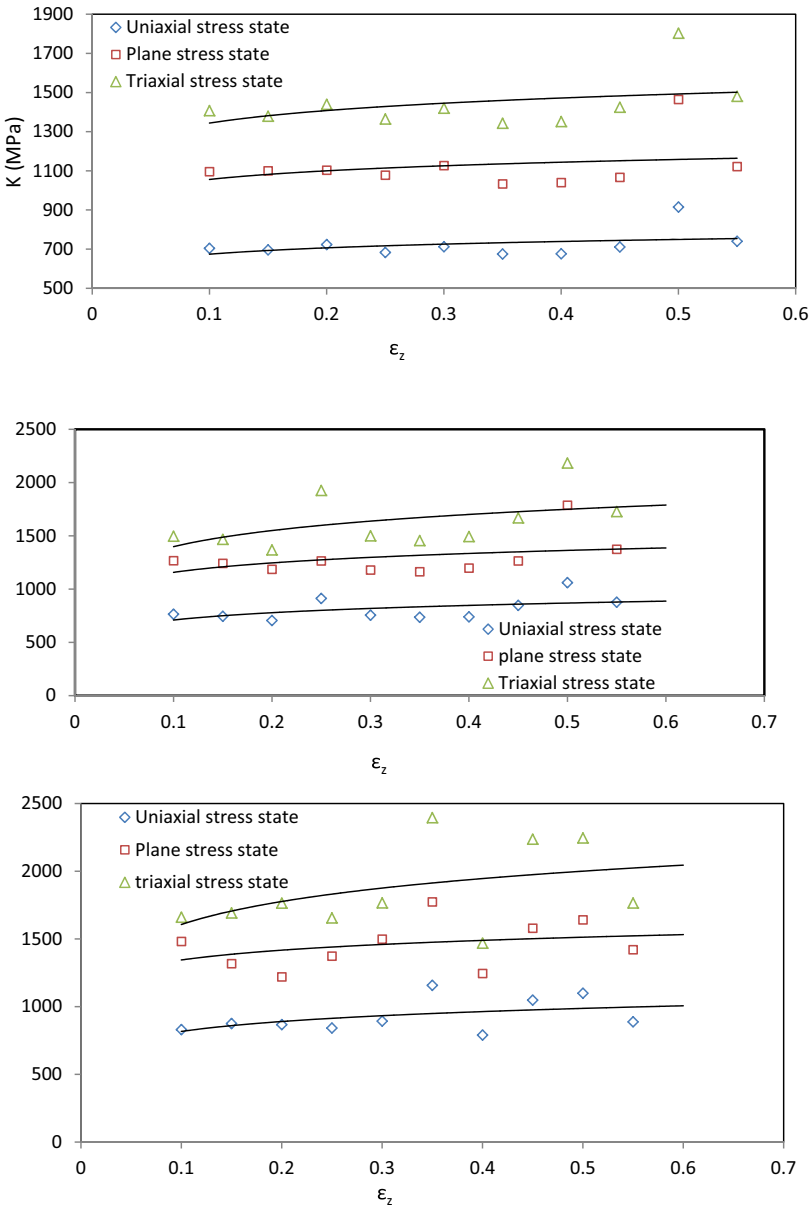

Fig. 4 Variation of instantaneous value of K with the axial strain for *a* h/d=1, *b* h/d=0.75, and *c* h/d=0.5

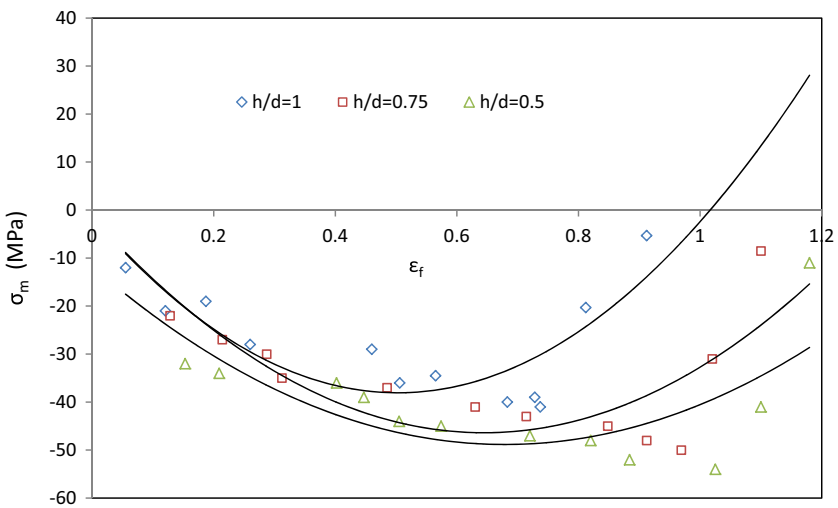

Fig. 5 Hydrostatic stresses (σ_m) versus effective strain (ε_f) for different h/d ratios

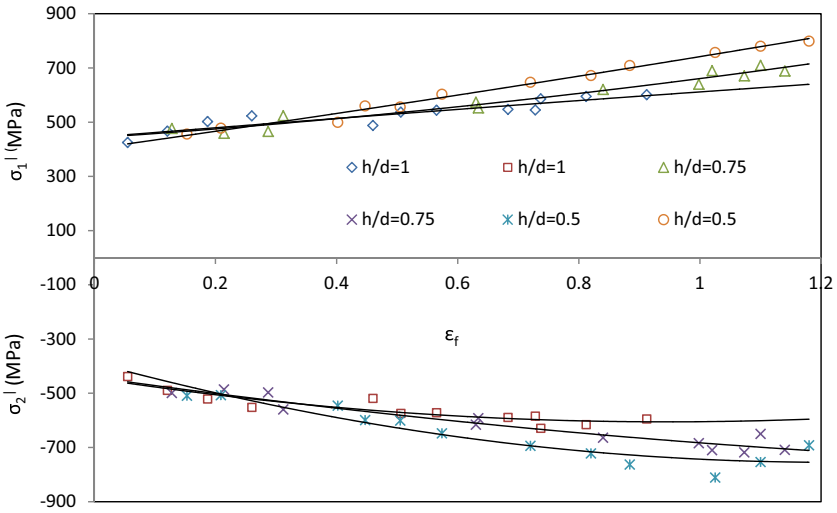

Fig. 6 Deviatoric stresses versus effective strain (ε_f) for different h/d ratios

failure were investigated. Figure 5 illustrates the plot of variation of hydrostatic stresses with respect to the effective strain. The value of hydrostatic stress is found to be compressive till the material reaches the fracture limit. At this stage of the process, the effective strain of the billet corresponding to the aspect ratios h/d=1, h/d=0.75, and h/d=0.5 are 0.91, 1.09, and 1.18, respectively. This improves the formability of the material irrespective of all the h/d ratios. The reason behind the better formability of the aspect ratio h/d=0.5 is because the increasing h/d ratios lead to buckling of the material at lower strains compared to the lower aspect ratios. The compressive nature of the hydrostatic stress is observed till the crack initiation. On further deformation, the crack propagates and the hydrostatic stress tries to become tensile in nature. Once the material starts cracking, the load required for deforming the material to higher strains decreases. This decreases the axial stress and from Eq. (A8), it can be said that the tensile nature of the hydrostatic stress has been increasing. This is no longer carried away by the barreled specimen, and finally, the material fractures. The trend lines of Fig. 5 clearly explain this phenomenon.

The tensile nature of the deviatoric stress $\sigma_1{}^{|}$ can be clearly examined in Fig. 6. It is tensile at the beginning of the process and remained as tensile even after crack initiation and propagation. The deviatoric stress $\sigma_2{}^{|}$ is compressive in nature till the crack initiation and turns to tensile slightly. This is because of the conjunction of the tensile axial stress (σ_z) with the tensile hydrostatic

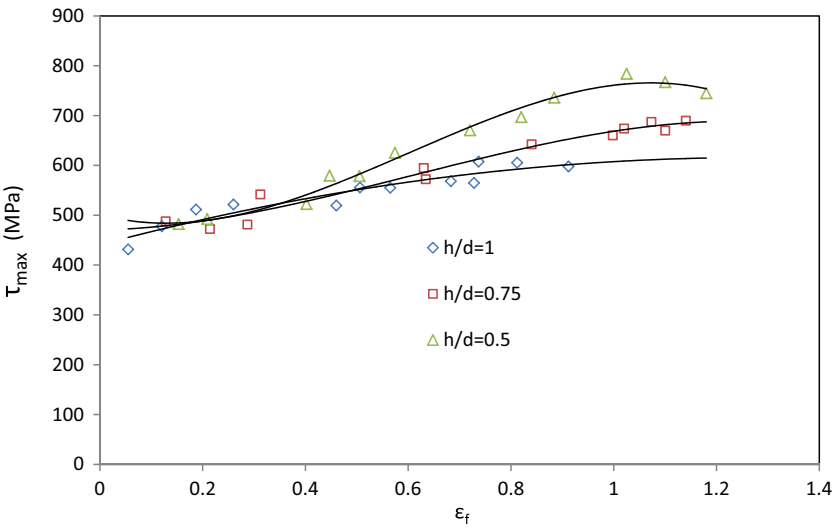

Fig. 7 Maximum shear stresses (τ_{max}) versus effective strain (ε_f) for different h/d ratios

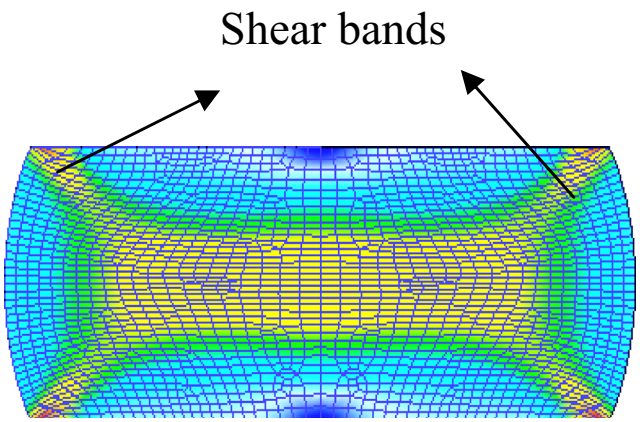

Fig. 8 Formation of shear bands

stress (σ_m). The high tensile stresses near the equatorial region influence the shape of the geometry irrespective of all the h/d ratios.

The failure predicted based on the maximum shear stress is plotted as Fig. 7. An increase in the amount of the effective strain increases the value of the shear stress. The crack starts initiating when the shear band moves along the plane of dead zone. A further increase in the level of deformation fractures the material at an angle of 45°. The fracture is caused by the localized shear band which fractures the billet at an angle 45° as illustrated in Fig. 8.

The slope of the trend lines of Fig. 7 is increasing with the increasing effective strain and tries to dip slightly at the end of the deformation process. The stress path followed by the billet depends on the aspect ratios as illustrated in Fig. 8. With the increase in the hydrostatic stress, the hoop stress is also increasing. A diversion in the path followed by different aspect ratios can be examined in Fig. 9. The point at which the curve has changed the direction is the value of the hydrostatic stress and hoop stress at which the fracture has initiated. An increase in the level of deformation decreases the magnitude of the axial stress, but still, the hoop stress goes on increasing. The decreases in the magnitude of the axial stress make the curves to turn back, and the curves are also creeping up because of the increase in the hoop stress.

Figure 10 illustrates that an increase in the axial loading has increased the axial stress (compressive), and the value of the axial stress turned tensile after fracture initiation. This made the hydrostatic stress to increase at the beginning of the process which has improved the formability of the material and its tensile nature made the billets to fracture irrespective of all the h/d ratios.

As explained above that the tensile nature of stresses near the equatorial region promotes fracture, a special focus has been made on the diameter bulged due to these stresses near the billet center. The increase in the compressive nature of the hydrostatic stress has increased the bulged diameter (Fig. 11). When the billet has fractured, a small decrement in the hydrostatic stress (tensile hydrostatic stress) has made a larger difference in the value of the bulged diameter. This clearly indicates the effectiveness of the hydrostatic stress on the formability of the material.

Until the crack has initiated, the deviatoric stress $\sigma_2{}^{|}$ is compressive and did not affect the shape of the geometry. As soon as the fracture has started, the value has become tensile in nature. In addition to value of $\sigma_2{}^{|}$, the increasing value of the deviatoric stress $\sigma_1{}^{|}$ leads to the bulging of the diameter at the center of the billet

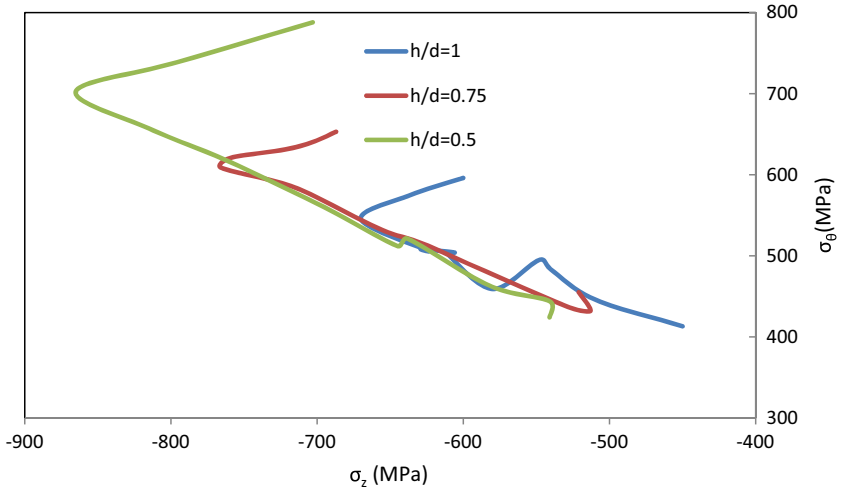

Fig. 9 Axial stress (σ_z) versus hoop stress (σ_θ) stress path for critical points for different h/d ratios

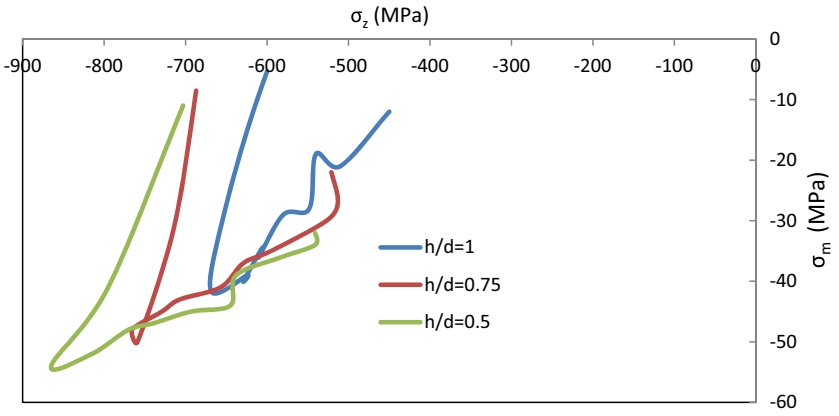

Fig. 10 Axial stresses (σ_z) versus hydrostatic (σ_m) stress path for critical points for different h/d ratios

and distorting the shape of the geometry. This phenomenon depends upon the h/d ratios as illustrated in Fig. 12.

At any stage of the process, with the increase in the level of deformation, the diameter at the center of the billet is going to increase. But the dependability of the rate of diametral expansion with the increasing effective strain depends on the tensile stresses near the equator of the billet. When subjected to the same amount of axial stress, the rate of change of bulged diameter with respect to the axial stress is more in case of h/d=1 than h/d= 0.75 and h/d=0.5. The increase in the compressive nature of the axial stress has increased the bulged diameter, but it becomes more severe when the axial stress turns tensile (Fig. 13).

3.3 Criterion based on void failure

The nucleation, elongation, and coalescence of voids may cause fracture in ductile materials up on severe plastic deformation. Based on the energy release rate, Lemaitre et al. [21] proposed an Eq. (8) which gives void failure.

$$Y = \frac{\sigma_{\text{eq}}^2}{2E(1-D)^2} V_D \tag{8}$$

$$V_D = \left[\frac{2}{3}(1+\nu) + 3(1-2\nu)\left(\frac{\sigma_m}{\sigma_{\text{eq}}}\right)^2\right] \tag{9}$$

In Eq. (2), V_D is the volume fraction of the voids, ν is the poisons ratio, and σ_{eq} is the equivalent stress. Based on the theory of continuous damage mechanics, Gurson [22] developed an expression for the failure of micro voids. Tvergaard and Needleman [23] modified Gurson's equation and developed a new yield function.

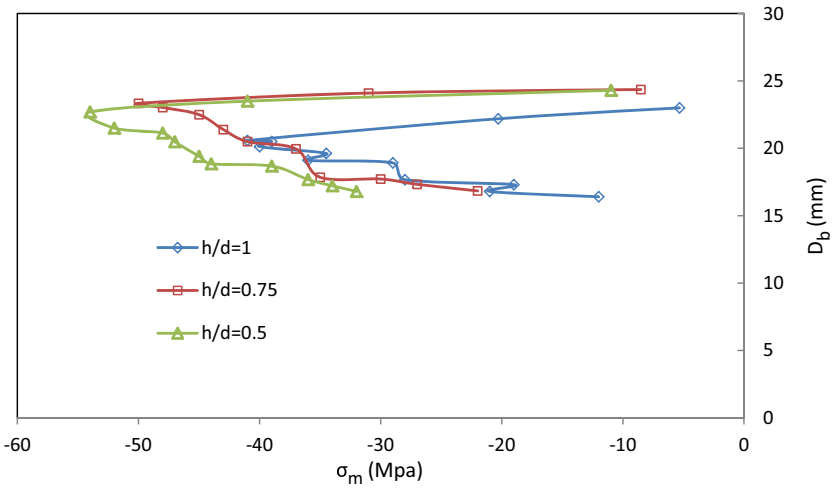

Fig. 11 Hydrostatic stress (σ_m) versus bulged diameter (D_b) for different aspect ratios

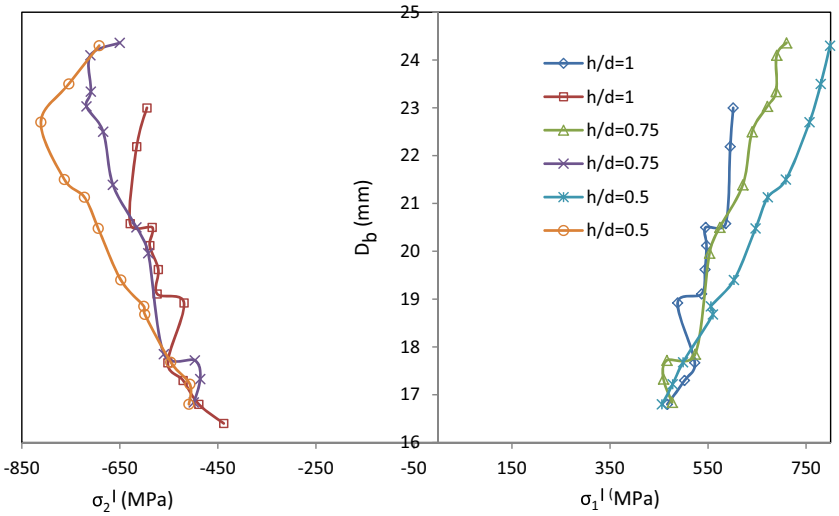

Fig. 12 Deviatoric stresses versus bulged diameter (D_b) for different aspect ratios

$$\phi = \left(\frac{\sigma_{eq}}{\sigma_M}\right)^2 + 2q_1 f^* \mathrm{COSh}\left(\frac{3q_2\sigma_m}{2\sigma_M}\right) - \left[1 + \left(q_1 f^*\right)^2\right] = 0 \tag{10}$$

σ_M is the yield stress of the undamaged material. σ_{eq} and σ_m are the equivalent stress and mean stress, respectively.

Upon considering q_1=1.5 and q_2=1, Tvergaard improved the solution accuracy of the yield function. The void volume fraction f^* is defined as

$$f^*(f) = \begin{cases} f & \text{for} \quad f \le f_c \\ f_c + \dfrac{1/q_1 - f_c}{f_f - f_c} & \text{for} \quad f_c \le f \le f_f \end{cases} \tag{11}$$

where f_c and f_f are the critical void fraction and the void volume fraction at fracture, respectively. The evolution of f is a sum of the nucleation (f^N) and growth (f^G) mechanisms:

$$f = f^N + f^G \tag{12}$$

The nucleation mechanism in this case is driven by plastic strain:

$$f^N = A\varepsilon_{eq}^p \tag{13}$$

where ε_{eq}^p is the equivalent plastic strain rate; parameter A is a scalar constant concerning the damage acceleration. It is estimated by the following expression:

$$A = \frac{f_N}{S_N\sqrt{2\pi}} \exp\left[-\frac{1}{2}\left(\frac{\varepsilon_{eq} - \varepsilon_N}{S_N}\right)^2\right] \tag{14}$$

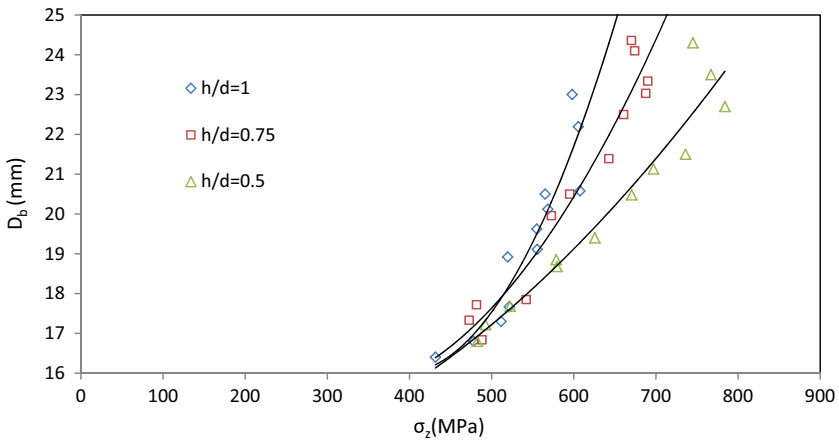

Fig. 13 Axial stresses versus bulged diameter (D_b) for different aspect ratios

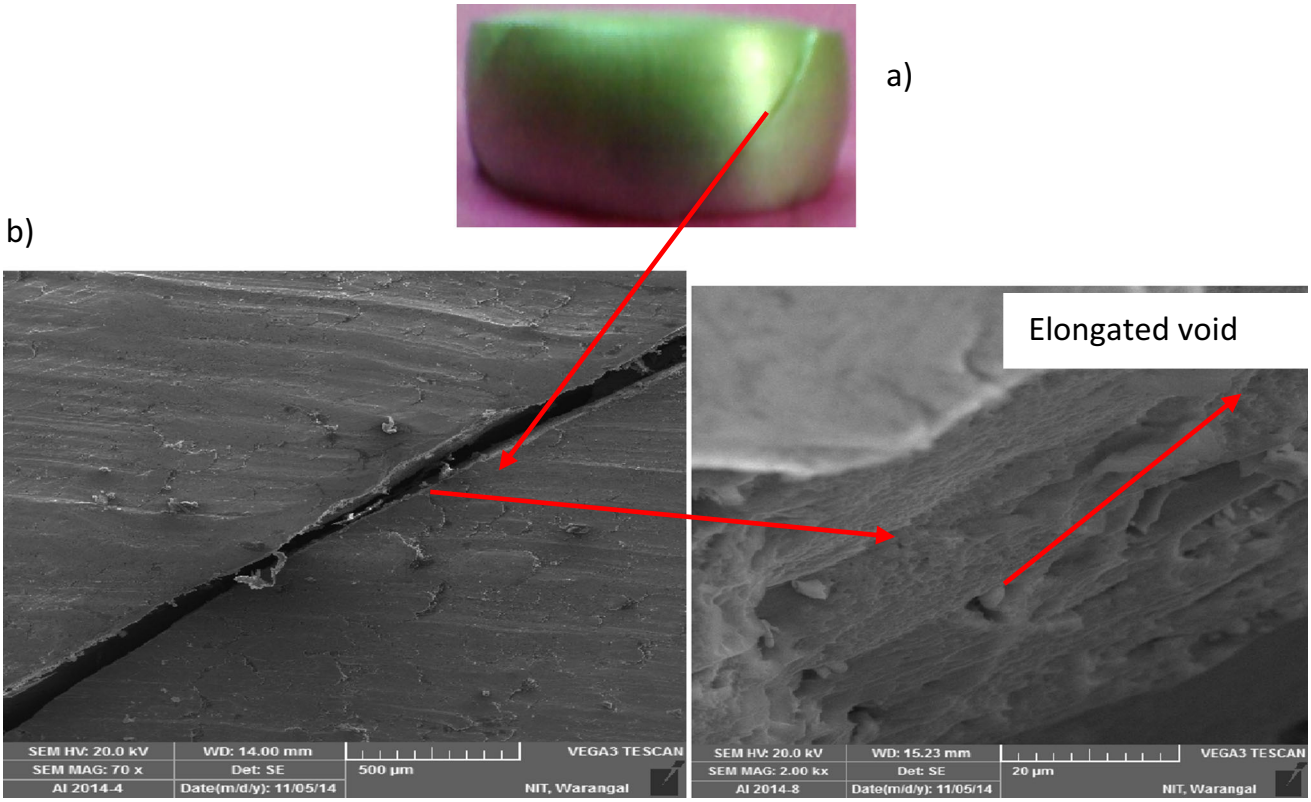

Fig. 14 Cracked billet **a** experimental result and **b** SEM image of elongated voids

where f_N is volume fraction of void nucleation particles, ε_N is the mean void nucleation strain, and S_N is the corresponding standard deviation.

The growth of the micro voids can be estimated by

$$f^G = (1-f)\overline{\varepsilon_p} \tag{15}$$

where $\overline{\varepsilon_p}$ is the strain rate of the plastic part.

Xue [24] replaced the void volume fraction f^* with the damage variable D and assumed that fracture occurs when the quantity $q_1 f^* = D$, Eq. (4) can be written as

$$\phi = \left(\frac{\sigma_{eq}}{\sigma_M}\right)^2 + 2D\mathrm{COS}h\left(\frac{3q_2\sigma_m}{2\sigma_M}\right) - \left(1+D^2\right) = 0 \tag{16}$$

Hill [25] proposed an anisotropic yield criterion based on the von Mises criterion.

$$\sqrt{\sigma_1^2 + \sigma_2^2 - \left(\frac{2R}{R+1}\right)\sigma_1\sigma_2} = \sigma_{eq} \tag{17}$$

Table 1 Damage criterion for void models

GTN model	Modified GTN model
$\phi = \left(\frac{\sigma_{eq}}{\sigma_M}\right)^2 + 2D\mathrm{COS}h\left(\frac{3q_2\sigma_m}{2\sigma_M}\right) - \left(1+D^2\right) = 0$	$\phi = \left(\frac{\sqrt{\sigma_1^2+\sigma_2^2-\left(\frac{2R}{R+1}\right)\sigma_1\sigma_2}}{\sigma_M}\right)^2 + 2D\mathrm{COS}h\left(\frac{3q_2\sigma_m}{2\sigma_M}\right) - \left(1+D^2\right) = 0$
Lemaitre model	Modified Lemaitre Model
$Y = \frac{\sigma_{eq}^2}{2E(1-D)}{}^2 V_D$	$Y = \frac{\sigma_{eq}^2}{2E(1-D)}{}^2 \left[\frac{2}{3}(1+\nu) + 3(1-2\nu)\left(\frac{\sigma_m}{\sqrt{\sigma_1^2+\sigma_2^2-\left(\frac{2R}{R+1}\right)\sigma_1\sigma_2}}\right)^2\right]$

Table 2 Material upset till fracture with different anisotropy ratios and effective strains

Material	K	n	R	ε
AISI 1040 carbon steel [26]	1320	0.226	0.33	0.81
Brass [27]	910	0.209	0.38	0.92
Al-6061-T6 [13]	561	0.11	0.5	1.22
AA2014-T6	720	0.22	0.42	1.13

where $R = \frac{\ln\left(\frac{d_f}{d_0}\right)}{\ln\left(\frac{h_0}{h_f}\right)}$ is anisotropy ratio.

Figure 14 illustrates the cracked AA2014 billet after upsetting. The elongation of voids and failure due to shear is also clearly illustrated in Fig. 14b. To examine the effect of anisotropy factor R on the yielding of materials, the Vonmises equivalent stress in the Gurson-Tvergaard-Needleman (GTN) criterion and Lemaitre criterion was replaced with the Hill-Vonmises Eq. (17), and the modified equations are listed in Table 1.

To analyze the formability of the materials for different anisotropy ratios, the upsetting operation performed on different materials and their corresponding R values and effective strains were noted down in Table 2. It can be observed from Table 2 that the increase in the strength coefficient has lowered anisotropy factor and formability of the material. In order to explain the effect of anisotropy on the formability of the material, the effective strain (ε) at the instant of fracture has been noted down by varying the R values. The effective strain at the point of fracture can be calculated from the equation. The value of the damage at the onset of fracture was evaluated from the modified equations of GTN and Lemaitre fracture models. The critical damage versus effective strain distribution plots for different anisotropy ratios were constructed as illustrated in Figs. 15 and 16. It can be observed from Figs. 15 and 16 that the increase in the anisotropy ratio has increased the effective strain distribution, and the critical damage has also increased.

$$\sigma = K\varepsilon^n \tag{18}$$

$$\sqrt{\sigma_1^2 + \sigma_2^2 - \left(\frac{2R}{R+1}\right)\sigma_1\sigma_2} = K\varepsilon^n \tag{19}$$

4 Conclusions

1. The work hardening behavior of the billet depends on the geometry and state of stress.
2. The crack initiation and propagation vary with the aspect ratios of the billet and also on the mechanism of failure when subjected to the same amount of strain.
3. The tensile nature of the axial stress and hydrostatic stress promotes fracture for all the h/d ratios. The tensile nature of the deviatoric stresses distorts the shape of the billet.
4. The material anisotropy plays a vital role in the upsetting, and the increase in anisotropy ratio increases the formability.
5. The constitutive modeling of anisotropy factor with the GTN criterion and Lemaitre criterion successfully explained the influence of anisotropy on the formability, and results are in accordance with the established literature.

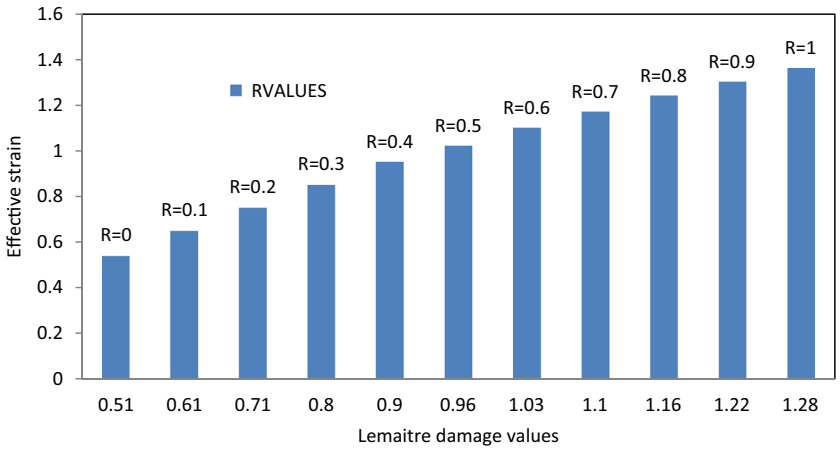

Fig. 15 Lemaitre damage parameter versus effective strain

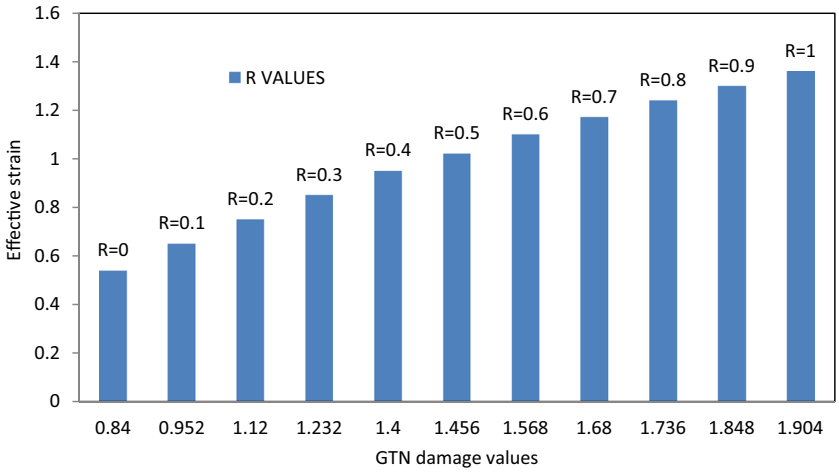

Fig. 16 GTN damage parameter versus effective strain

Appendix A

Uniaxial state of stress

According to Abdel-Rahman et al. [28]

$$\sigma_z = -\sigma_{\text{eff}},\ \sigma_r = \sigma_\theta = 0$$

where σ_z is the axial stress, σ_r, σ_θ, and σ_{eff} are the radial, hoop, and effective stresses, respectively

$$\sigma_z = \frac{\text{load}}{A_i} \tag{A1}$$

where A_i is the instantaneous contact area

$$\text{True axial strain} : \varepsilon_z = \ln\left(\frac{h_f}{h_o}\right) \tag{A2}$$

where h_f is the final height after deformation and h_o is the initial height of the billet

$$\text{Hoop strain} : \varepsilon_\theta = \frac{d_f}{d_o} \tag{A3}$$

where d_f is the final diameter after deformation and d_o is the initial diameter of the billet

$$\text{Hydrostatic stress } \sigma_m = \frac{\sigma_z}{3} \tag{A4}$$

Appendix B

Plane stress state condition

According to Sowerby et al. [29], the state of stress under plane stress condition is as follows:

$$\text{Hoop stress} : \sigma_\theta = \left[\frac{(1+2\alpha)}{(2+\alpha)}\right]\sigma_z \tag{A5}$$

$$\text{Effective stress} : \sigma_{\text{eff}} = \left[\frac{1}{(2+\alpha)}\right]\left[3\left(1+\alpha+\alpha^2\right)\right]^{0.5}\sigma_z \tag{A6}$$

where α is the Poisson's ratio

$$\alpha = \frac{\varepsilon\theta}{\varepsilon_z} \tag{A7}$$

$$\text{Hydrostatic stress} : \sigma_m = \frac{1}{3}(\sigma_\theta + \sigma_z) \tag{A8}$$

$$\varepsilon_{\text{eff}} = \frac{2}{\sqrt{3}}\left(1+\alpha+\alpha^2\right)^{0.5}\varepsilon_z \tag{A9}$$

Appendix C

Triaxial state of stress

According to Narayansamy and Ponalagusamy [30], the state of stress under the triaxial stress state condition is as follows:

$$\alpha = \frac{A}{B} \tag{A10}$$

$$A = [3\sigma_\theta - (\sigma_z + 2\sigma_\theta)] \tag{A11}$$

$$B = [3\sigma_z - (\sigma_z + 2\sigma_\theta)] \tag{A12}$$

where α is the strain increment ratio

$$\alpha = \frac{d\varepsilon_\theta}{d\varepsilon_z} \tag{A13}$$

From Eq. (12), the hoop stress is given by

$$\sigma_\theta = \left(\frac{2\alpha + 1}{1 + 2\alpha}\right)\sigma_z \tag{A14}$$

For axi-symmetric solids, it is assumed that $\sigma_r = \sigma_\theta$.

As explained elsewhere [31], the effective stress is written as follows:

$$\sigma_{\text{eff}}^2 = \sigma_1^2 + \sigma_2^2 + \sigma_3^2 - (\sigma_1\sigma_2 + \sigma_2\sigma_3 + \sigma_3\sigma_1) \tag{A15}$$

The expression can be written in terms of cylindrical coordinates as

$$\sigma_{\text{eff}}^2 = \sigma_z^2 + \sigma_\theta^2 + \sigma_r^2 - (\sigma_z\sigma_\theta + \sigma_\theta\sigma_r + \sigma_r\sigma_z) \tag{A16}$$

Since $\sigma_\theta = \sigma_r$ for cylindrical axi-symmetric upsetting

$$\sigma_{\text{eff}} = \left[\sigma_z^2 + 2\sigma_\theta^2 - \left(\sigma_\theta^2 + 2\sigma_z\sigma_\theta\right)\right]^{0.5} \tag{A17}$$

As explained elsewhere [31], the effective strain can be written as follows:

$$\varepsilon_{\text{eff}} = \left[\frac{2}{3}\left(\varepsilon_z^2 + \varepsilon_\theta^2 + \varepsilon_r^2\right)\right]^{0.5} \tag{A18}$$

References

1. Baskaran K, Narayanasamy R (2008) An experimental investigation on work hardening behaviour of elliptical shaped billets of aluminium during cold upsetting. Mater Des 29:1240–1265
2. Narayanasamy R, Pandey KS (1998) Some aspects of work hardening in sintered aluminium–iron composite preforms during cold axial forming. J Mater Process Technol 84:136–42
3. Inigoraj AJR, Narayanasamy R, Pandey KS (1998) Strain hardening behaviour of sintered aluminium–3.5 % alumina composite preforms during axial compression with and without annealing. J Mater Process Technol 84:143–148
4. Selvakumar N, Narayansamy R (2003) Phenomenon of strain hardening behaviour sintered aluminium preforms during cold axial forming. J Mater Process Technol 142:347–54
5. Vettivel SC, Selvakumar N, Vijay Ponraj P (2012) Mechanical behavior of sintered Cu-5%W nano powder composite. Procedia Eng 38:2874–2880
6. Baskaran K, Narayanasamy R (2008) Effect of various stress ratio parameters on cold upset forging of irregular shaped billets using graphite as lubricant under plane and triaxial stress state conditions. Mater Des 29:2089–2103
7. Baskaran K, Narayanasamy R (2008) Some aspects of barrelling in elliptical shaped billets of aluminium during cold upset forging with lubricant. Mater Des 29:638–661
8. Malayappan S, Esakkimuthu G (2006) Barrelling of aluminium solid cylinders during cold upsetting with differential frictional conditions at the faces. Int J Adv Manuf Technol. doi:10.1007/s00170-005-2503-6
9. Malayappan S, Narayanasamy R (2004) An experimental analysis of upset forging of aluminium cylindrical billets considering the dissimilar frictional conditions at flat die surfaces. Int J Adv Manuf Technol. doi:10.1007/s00170-003-1584-3
10. Fuh-Kuo C, Cheng-Jun C (2000) On the nonuniform deformation of the cylinder compression test. J Eng Mater Technol 122:192–197
11. Alves LM, Nielsen CV, Martins PAV (2011) Revisiting the fundamentals and capabilities of the stack compression test. Exp Mech 51:1565–1572
12. Song Y, Xiaolong X, Jie Z, Zhen Z (2007) Ductile fracture modeling of initiation and propagation in sheet-metal blanking processes. J Mater Process Technol 187–188:169–172
13. Li H, Fu FW, Lu J, Yang H (2011) Ductile fracture: experiments and computations. Int J Plast 27:147–180
14. Kim DJ, Kim BM (2002) Prediction of deformed configuration and ductile fracture for simple upsetting using an artificial neural network. Int J Adv Manuf Technol 19:336–342
15. Andrade Pires FM, Cesar-de-Sa JMA, Costa-Sousa L, Natal-Jorge RM (2003) Numerical modelling of ductile plastic damage in bulk metal forming. Int J Mech Sci 45:273–294
16. Gouveia BPPA, Rodrigues JMC, Martins PAF (2000) Ductile fracture in metalworking: experimental and theoretical research. J Mater Process Technol 101:52–63
17. Cockcroft MG, Latham DJ (1968) Ductility and the workability of metals. J Inst Met 96:33
18. Freudenthal FA (1950) The inelastic behavior of engineering materials & structures. John Wiley & Sons, New York
19. Brozzo P, Deluca B, Rendina R (1972) Proceedings of the Seventh Biennial Conference of the International Deep Drawing Research Group. Amsterdam, Netherlands
20. Abdel-Rahman M, El S (1995) Workability in forging of powder metallurgy compacts. J Mater Process Technol 54:97–102
21. Lemaitre J (1986) Local approach of fracture. Eng Fract Mech 25:523–537

22. Gurson AL (1977) Continuum theory of ductile rupture by void nucleation and growth—part I. Yield criteria and flow rules for porous ductile media. J Eng Mater Technol 99:2–15
23. Tvergaard V, Needleman A (1984) Analysis of the cup-cone fracture in a round tensile bar. Acta Metall 32:157–169
24. Xue L (2008) Constitutive modeling of void shearing effect in ductile fracture of porous materials. Eng Fract Mech 75:3343–3366
25. Hill R (1948) A theory of the yielding and plastic flow of anisotropic metals. Proc R Soc A 193:260–281
26. Landre J, Pertence A, Cetlin PR, Rodrigues JMC, Martins PAF (2003) On the utilization of ductile fracture criterion in cold forging. Finite Elem Anal Des 39:174–186
27. Erman T, Ozgur K (2003) Analysis of formability of metals, Master Thesis, Graduate School of Natural and applied sciences, The Middle East Technical University, Turkey
28. Sowerby R, O'Reilly I, Chandrasekaran N, Dung NL (1984) Materials testing for cold forging. ASME J Eng Mater Technol 106:101–106
29. Narayanasamy R, Ponalagusamy R (2005) Unpublished report on P/M forging part-I. National Institute of Technology, Tiruchirappalli
30. Doraivelu SM, Gegel HL, Gunasekara JS, Malas JC, Morgan JT (1984) A new yield function for compressible P/M materials. Int J Mech Sci 26:527–35
31. Narayanasamy R (2005) Unpublished report on P/M forging part-II. National Institute of Technology, Tiruchirappalli